



# Fatigue Properties of Resistance Spot Welded Dissimilar Interstitial-Free and High Strength Micro-Alloyed Steel Sheets

Gorti Janardhan<sup>1</sup> · Kaushal Kishore<sup>2</sup> · Goutam Mukhopadhyay<sup>2</sup> · Krishna Dutta<sup>1</sup>

Received: 15 January 2020 / Accepted: 2 March 2020 / Published online: 19 March 2020  
© The Korean Institute of Metals and Materials 2020

## Abstract

This study aims to investigate the influence of nugget diameter on tensile-shear and fatigue properties of the dissimilar resistance spot-welded joints of interstitial free and high strength niobium microalloyed steel sheets. The spot-weldings are done at currents of 7 kA and 9 kA at welding time of 300 ms with electrode force of 2.6 kN. Fatigue tests are done at different load amplitudes, considering the maximum tensile-shear load bearing capacity of the joints. The tests are interrupted before the final failure to understand the crack initiation and propagation paths. The study is supplemented by the microstructural and detailed fractographic analyses. The results indicated that the fatigue strength of the spot-welds increased with a decrease in nugget diameter. This could be attributed to the higher microhardness of heat affected zone (HAZ), presence of compressive residual stress and lower variation in thickness reduction on the IF steel side, welded at 7 kA. However, the tensile-shear load bearing capacity of the spot-welds increased with increase in the nugget diameter. The failure of the spot-welded joint under static loading initiates from the HAZ/base metal interface of the IF steel side. Nevertheless, under cyclic loading crack initiates from the notch root at the interface of two sheets lying in the HAZ of IF steel side. Fractographic investigations indicate intergranular fracture features in combination with striations, secondary cracks on the IF steel side under cyclic loading. Fracture surfaces of the specimens failed under static loading shows however, shear dimples on the IF steel side.

**Keywords** Spot welds · Dissimilar metals · Fatigue behavior · Nugget diameter · Failure location

## 1 Introduction

Today automakers are striving towards making lighter-weight vehicles, reducing the fuel consumption and thereby lowering down the greenhouse emissions by extensive usage of thinner sheets [1]. Interstitial-free and high strength niobium microalloyed steels are amongst the most widely used grades of commercial steels used in the automotive industries [2], owing to their high strength, formability, and weldability [3]. In automotive industries, thin sheets in an autobody are mostly joined by the resistance spot welding process [4]. The investigations related to the response of spot welds under static and fatigue loading conditions are crucial in terms of vehicle crash-worthiness [5]. Under normal service period of

a car, the joints existing in the welded structure experiences different types of complicated loading histories i.e. tensile shear, cyclic and torsional loadings [6]. Damages due to random fatigue loading occur primarily due to rough roads, vibrations, noise, and harshness, these factors apply periodical overloads to the vehicle. Hence, it appears that fatigue strength of the spot-welded joints governs the overall structural integrity, durability, and safety of a vehicle [7]. In automobiles, significant numbers of the joints are made up of dissimilar grades of steels with different sheet thicknesses. The spot-welded joint provides local connections to the welded components in the assembled body in white. They act as inherent circumferential notches, leading to higher stress concentrations at these locations, and consequently making the structures susceptible to fatigue failures. The majority of the failures in the automotive components under cyclic loading mostly occur around the spot-welded joints [8–10]. Therefore, it necessitates preventing the fatigue failures of the spot-welds at the time of designing the vehicles. Although there exist a large number of applications of dissimilar resistance spot-welded joints, limited reports exist

✉ Gorti Janardhan  
g.janardhan@hotmail.com

<sup>1</sup> Department of Metallurgical and Materials Engineering,  
National Institute of Technology, Rourkela 769008, India

<sup>2</sup> R&D and Scientific Services, Tata Steel Limited,  
Jamshedpur 831001, India

dealing with the mechanical performance of high strength niobium (HSNb) microalloyed and interstitial free steel (IF) spot-welded joints. Hence, it becomes necessary to study fatigue behaviour of the dissimilar combinations of IF and HSNb steel sheets. In the recent past, several studies related to the fatigue behaviour of spot-welded joints for similar combinations of steels have been carried out. Rathbun et al. reported that the microstructure and tensile properties of the parent materials have no influence on the fatigue strength of three similar combinations of spot-welded high strength bare steels (HSLA, DP, and TRIP). The fatigue properties of the joints are primarily influenced by three factors namely, sheet thickness, nugget diameter, and stresses developed around the weld [11]. Zhang and Taylor found that the number of loading cycles to failure is dependent on the sheet thickness and properties of the material under loading [12]. Banerjee et al. investigated the effect of nugget size on the fatigue properties of the spot-welded dual phase steel sheets. They showed that with an increase in nugget size the fatigue performance of the spot-welds increases. At higher load and lower number of cycles, the tendency for the occurrence of interfacial failure is significantly higher compared to that of lower load and a higher number of cycles. This is attributed to poor metallurgical bonding and higher shear stresses at the interface of two sheets at higher loads [13]. Long and Khanna reported the fatigue properties of the spot-welded HSLA steels. They showed that the failure of the spot-welds under fatigue loading is highly dependent on notch geometry and stresses acting at the inherent circumferential notch [14]. Ghosh and Pal reported the effect of strength and base metal on the fatigue behavior of spot-welded IF steels. It was shown that the fatigue strength of the high strength IF steel with lower sheet thickness is higher compared to the IF steel with lower strength and higher thicknesses in the elastic domain [15]. However, there is a scarcity of studies in the open literature that discusses high cycle fatigue behavior of the spot-welded IF and HSNb steel sheets. Therefore, the current study is directed towards assessment of fatigue properties of dissimilar combinations of resistance spot-welded steel joints i.e. IF and HSNb microalloyed steels subjected

to sinusoidal tensile-shear loads. The effect of nugget diameter on the fatigue properties of the spot-welded joints has also been examined. Additionally, microstructural evolution, determination of microhardness profiles, failure location and fractographic examination has also been carried out in detail. The fatigue crack initiation and propagation paths have been investigated by interrupted fatigue tests.

## 2 Experimental Procedure

### 2.1 Material

The thicknesses of the selected HSNb and IF steel sheets are 1.2 mm. The chemical compositions of the steels are summarized in Table 1. The tensile properties of the as-received steel sheets are presented in Table 2.

### 2.2 Spot-Welding Procedure and Test Configuration

The spot welding of the dissimilar combinations of the steel sheets has been carried out on a 150 kVA pedestal based medium frequency direct current machine (MFDC) following BS1140:1993. The welding process parameters selected for the current study are given in Table 3. The specimens of lap-shear configuration have been prepared with the standard dimension of 105 mm × 45 mm with an overlap length of 35 mm and two flat metal stiffeners of 45 mm × 35 mm were placed at two ends of the welded lap-shear joint to avoid nugget rotation and bending during fatigue testing. The measurement of residual stress at the heat affected zone has been carried out for the spot-welded joints at different welding currents (7 kA, 9 kA). For this, X-ray diffraction studies on selected specimens have been conducted using Co-K $\alpha$  radiation. First, the positions of high intensity peaks have been determined at a scan rate of 10°/min, followed by this a very slow scan rate (with angular steps of 0.02° and counting time of 25 s) has been employed at the highest intensity peak. The stress measurement has been done using Expert Stress software.

**Table 1** Chemical composition (wt%) of the investigated HSNb and IF steel

Steels	C	Mn	S	P	Si	Al	Cr	Ni	Ti	Nb	N	Fe
HSNb	0.039	1.45	0.006	0.023	0.007	0.042	0.018	0.016	0.001	0.012	0.0019	Bal.
IF	0.002	0.10	0.008	0.010	0.002	0.073	0.012	0.016	0.054	0.001	0.0024	Bal.

**Table 2** Tensile properties of HSNb and IF steels

Steel	Yield strength (MPa)	Ultimate tensile strength (MPa)	Uniform elongation (%)	Total elongation (%)
HSNb	312 ± 3.05	442 ± 4	14.08 ± 3	26.19 ± 1.5
IF	144 ± 2.08	275 ± 5	27.25 ± 2.5	49.46 ± 2

**Table 3** Spot-welding parameters

Weld current (kA)	Weld time (ms)	Squeezing time (ms)	Holding time (ms)	Electrode force (kN)	Cooling time (L/min)	Electrode shape and material	Face diameter (mm)	Shank diameter (mm)
7, 9	300	900	200	2.6	4	Truncated cone Cu–Cr–Zr	6	16

### 2.3 Macro- and Microstructures

The metallographic examinations of the spot-welded joints have been carried out by cutting the specimens just above the weld centre line using a slow speed cutter. The cross-sectional parts of the spot-welded joints have been mounted and polished using the standard metallographic procedure. The macro- and microstructural changes in the distinct regions of the welded joints have been observed using an optical microscope (Model: Leica DM6000M, Germany) and scanning electron microscope (Model: Carl Zeiss Supra 25, Germany). The nugget diameters formed at different welding parameters have been estimated using a stereo microscope (Model: Leica 205A, Germany) by measuring the dimensions of the weld cross-sections. The average nugget diameters of the three welded joints have been considered.

### 2.4 Microhardness Testing

The microhardness profiles across the welded joint have been examined just above the weld centreline using EMCO Vickers microhardness tester (Model: EMCO DuraScan 20GS, Austria). For this, hardness values have been measured in the transverse direction of the welded joint. The applied load is 100 g with a dwell time of 15 s; indentations have been

made with equal intervals at a distance of 0.26 mm. The indentations were taken at a distance of more than 3.5 times the diagonal size of the indentation, following the ASTM standard.

### 2.5 Tensile-Shear Testing

Tensile-shear type specimens as schematically shown in Fig. 1a have been tested between the flat grips on Instron servo-electric universal testing machine (Model: Instron 5582, UK) of capacity 100 kN, with a cross-head velocity of 5 mm/min at room temperature. The maximum tensile-shear load ( $P_{ts}$ ) sustained by spot-welded joints until pull out failure has been determined from the typical load–displacement curve obtained during tensile-shear testing. The average of three readings with standard deviations has been considered. The energy absorbed by the joints has been determined by integrating the area under the load-extension curve until the maximum tensile-shear load ( $P_{ts}$ ) sustained by the joints.

### 2.6 Fatigue Testing

The high cycle fatigue tests of the tensile-shear (TS) specimens have been carried out on the resonance type universal testing machine (Model: Instron 8800, UK) with a capacity of 100 kN.

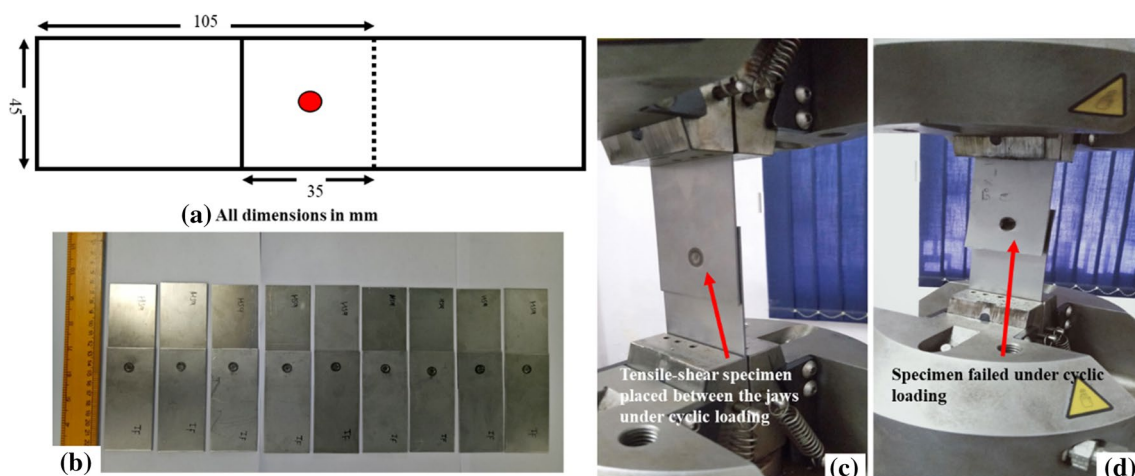


**Fig. 1** a Schematic of the spot-welded tensile-shear (TS) specimen, b fabricated spot-welded specimens and c TS specimen between jaws before fatigue testing, and d complete failure of TS specimen subjected to cyclic loading

The fabricated spot-welded specimens for fatigue testing are exhibited in Fig. 1b. The specimens have been tightened between the two grips as shown in Fig. 1c before the testing. The typical failed tensile-shear joint specimen under cyclic loading is shown in Fig. 1d. These specimens have been subjected to sinusoidal loads with load ratio  $(R)=0.1 = \frac{P_{min}}{P_{max}}$  at a frequency of 15 Hz for each fatigue test. Here  $P_{min}$  and  $P_{max}$  refers to the minimum and maximum applied loads respectively. The maximum load ( $P_{max}$ ) of the fatigue test has been varied from 50% to 10% of the maximum tensile-shear load ( $P_{ts}$ ) obtained during a tensile-shear test. For each test condition, at least three specimens have been tested and the average number of cycles to failure ( $N_f$ ) has been considered. Interrupted fatigue tests have been carried out on the spot-welded joints at 40% of the maximum tensile-shear load ( $P_{ts}$ ) equivalent to 3.32 kN. The tests have been carried out at designated percentages (20%, 30%, and 50%) of the number of cycles to failure ( $N_f$ ) to determine the location of crack initiation and its propagation at various stages of the cyclic loading.

**2.7 Post Failure Examination**

The fractured surfaces of welded joints have been examined under the field scanning electron microscope (Model: FEI Nova NanoSEM 430, USA) to characterize the detailed features of the cracked surfaces. The location of failure for the specimens after tensile-shear (TS) and fatigue testing at different welding currents were determined by preparing the cross-section of the broken specimens by cutting just above the weld centerline. Finally, they were mounted and polished using standard metallography procedures.

**3 Results and Discussion**

**3.1 Macro- and Microstructural Evolution of the Welded Joints**

The macrostructural views of typical spot-welded IF/HSNb joints are shown in Fig. 2a, b. It is observed that the joints consist of three distinct regions, commonly known as fusion

zone (FZ), heat affected zone (HAZ), and the base metal (BM) respectively [16]. The nugget diameter (D) refers to the dimension of the elliptical nugget present in the central portion of the welded joint. It is observed that the nugget diameter at a welding current of 9 kA is greater than that of 7 kA due to higher heat input [17]. The plot of sheet thickness reduction (due to electrode indentation) of the IF/HSNb joints at different welding currents is shown in Fig. 3. The electrode indentation marks on the IF steel side and HSNb steel side at different welding currents is shown in Fig. 4. It is observed that at higher welding current (9 kA) the sheet thickness reduction is maximum in both IF and HSNb steel side as compared to that of the lower welding current (7 kA). It is well known that higher the welding current, more is the weld nugget diameter and higher is the electrode indentation [18, 19]. Besides, the electrode indentation is also controlled by the electrode pressure, temperature of the electrode/sheet interface, and contact resistance between sheet/sheet interface, and electrode/sheet interface. The increase in heat input leads to increase in the temperature at the electrode sheet

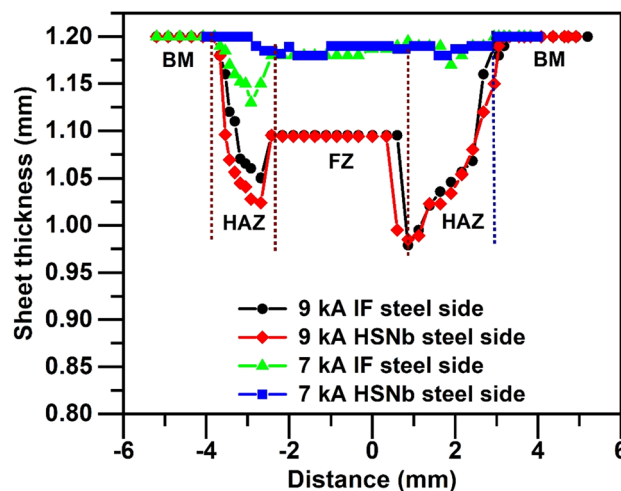
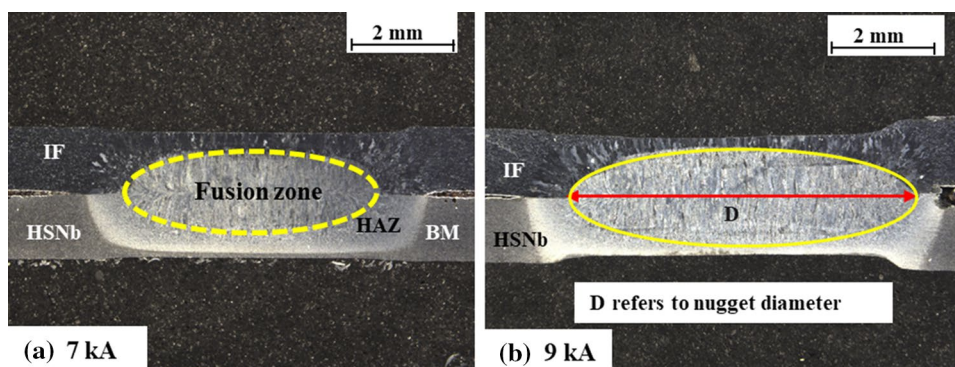
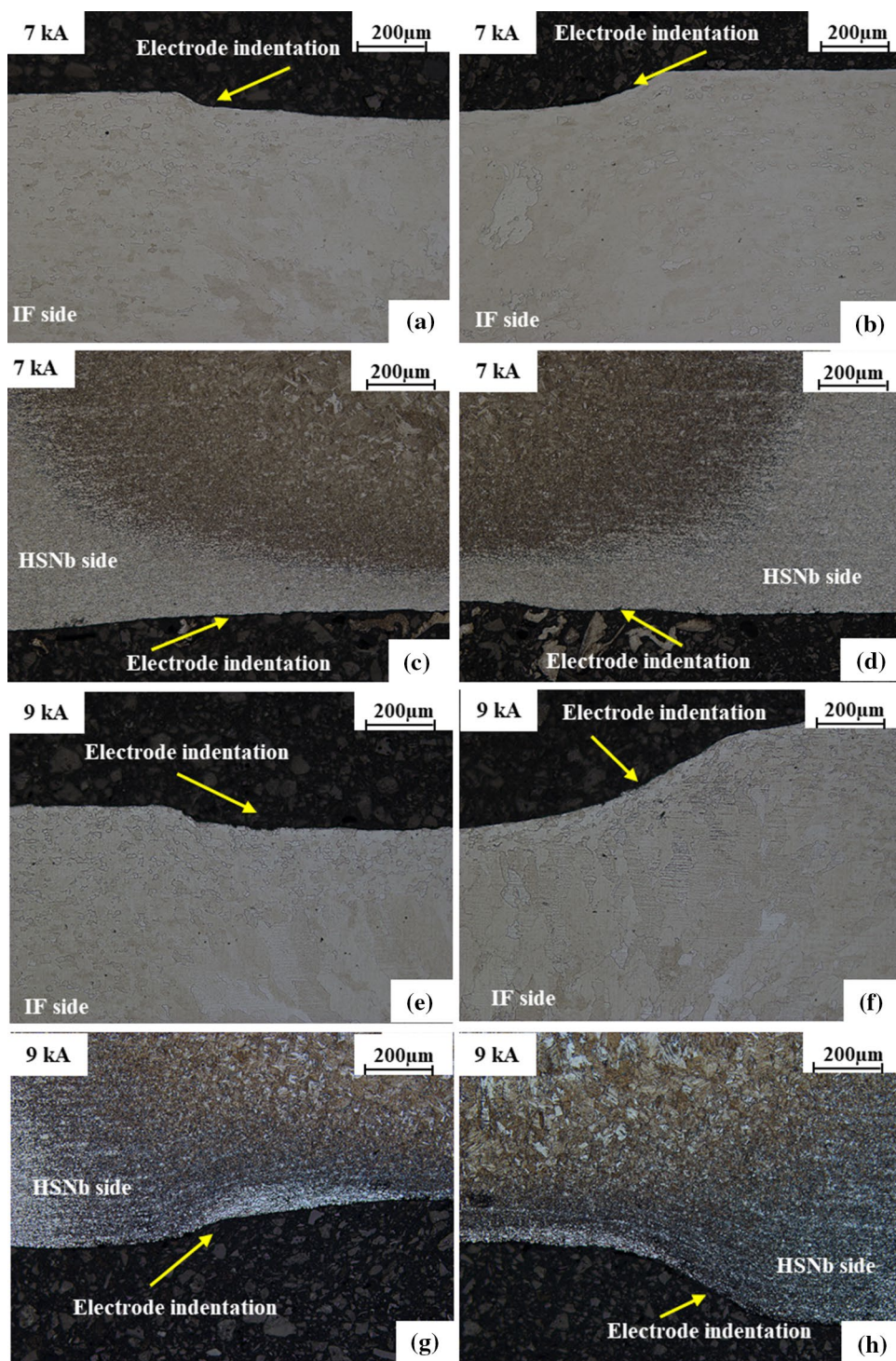


Fig. 3 Plot of sheet thickness reduction profile across the joints at different welding currents

Fig. 2 Schematic of cross-section of the weld joints at different welding currents: a 7 kA, b 9 kA



**Fig. 4** Micro views of the IF/HSNb joints showing electrode indentation marks on IF and HSNb steel side of the joints at different welding currents; **a–d** refers to 7 kA and **e–h** refers to 9 kA

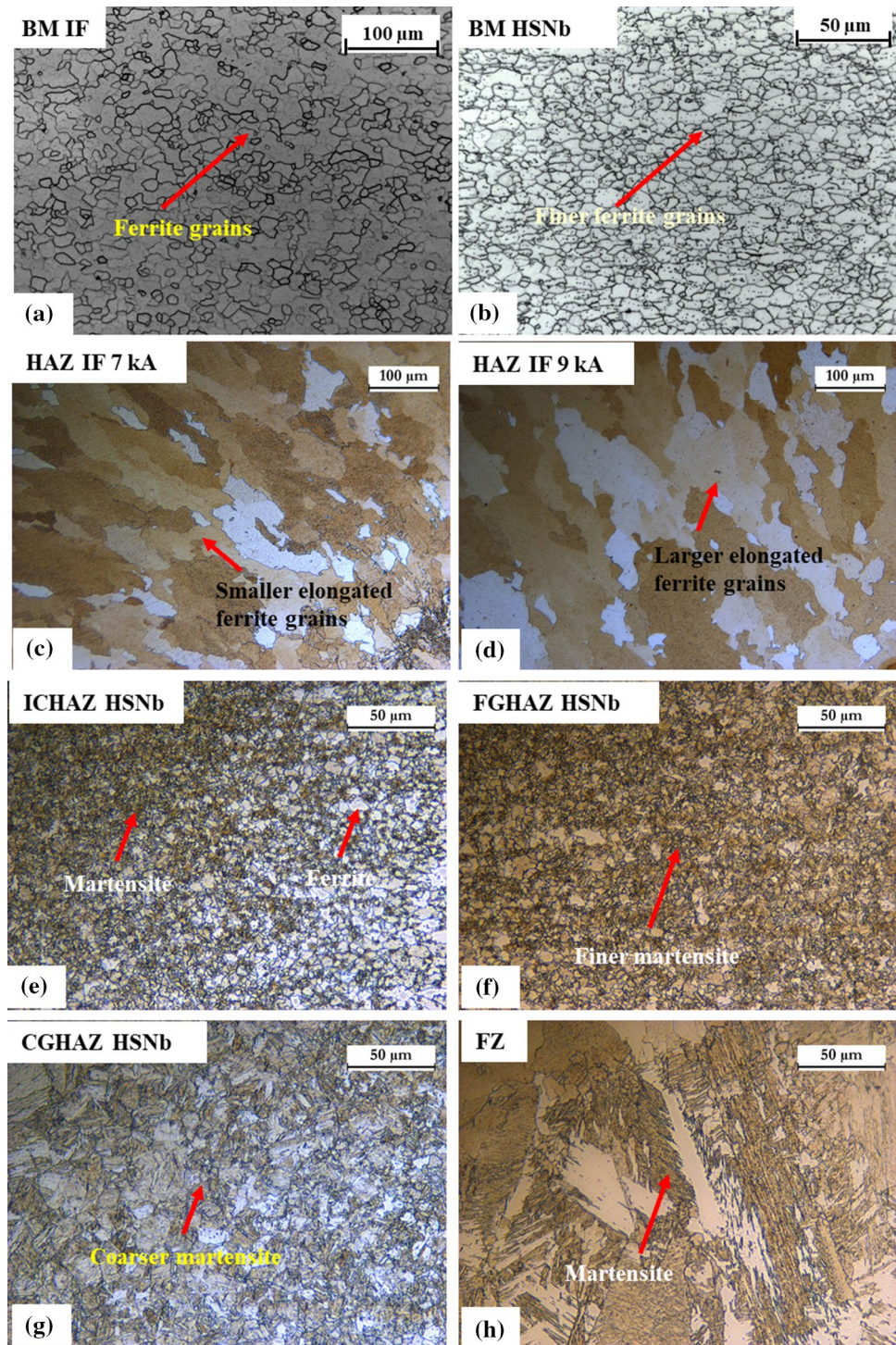


interface, which increases the degree of plastic deformation that can occur on the surface of the sheet subjected to electrode pressure.

The microstructures formed in the different regions of IF/HSNb steel spot-welded joints are shown in Fig. 5a–h. The microstructure of the IF steel base metal is shown in Fig. 5a, that predominately consists of ferrite grains with

the average grain size of  $23 \pm 0.5 \mu\text{m}$  and likewise, the HSNb steel contains finer ferrite grains of average grain size  $10 \pm 0.4 \mu\text{m}$  with precipitates at the grain boundaries as observed in Fig. 5b. The HAZ of the IF steel side at different welding currents (7,9 kA) is shown in Fig. 5c, d. They consist of elongated ferrite grains as shown in Fig. 6a because of annealing-like effect during cooling for

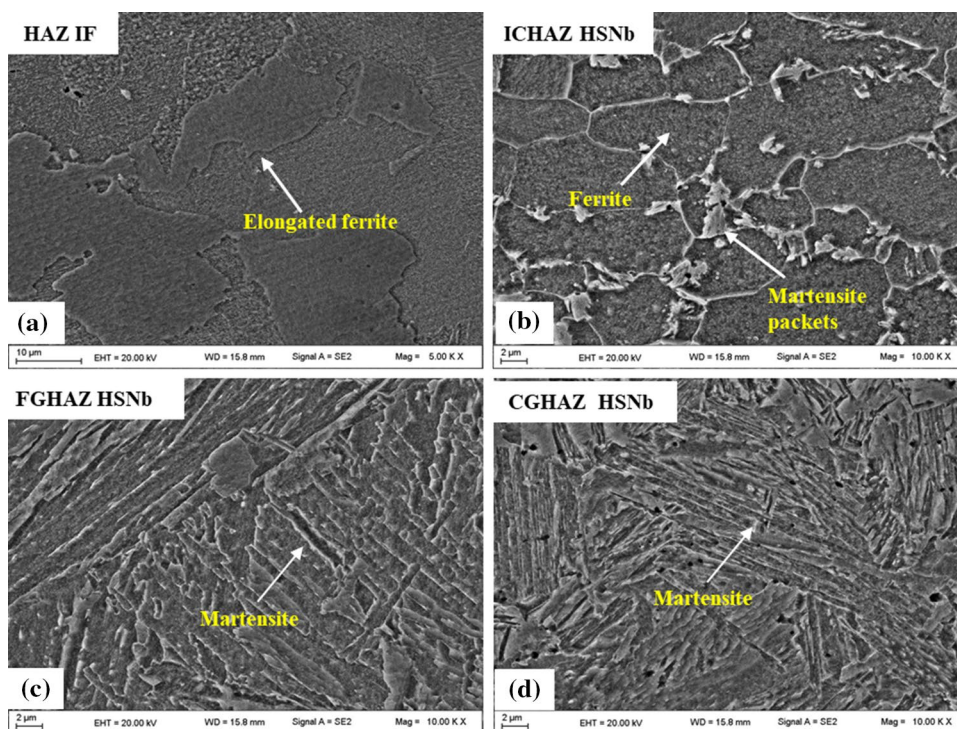
**Fig. 5** Microstructures of the IF/HSNb joint refers to **a** IF base metal, **b** HSNb base metal, **c, d** HAZ IF side at welding currents of 7 kA and 9 kA **e** ICHAZ HSNb side, **f** FGHAZ HSNb side, **g** CGHAZ HSNb side, and **h** FZ respectively



a longer duration. It is interesting to note that at higher current (9 kA) the ferrite grains are coarser in nature as compared to that of lower welding current (7 kA). Typical ferrite grain size (in longitudinal direction) in HAZ is estimated as  $132.9 \pm 35.8 \mu\text{m}$  for the lower current (7 kA) specimen however it is  $182.1 \pm 48.1 \mu\text{m}$  for the higher current (9 kA) specimen. These results are in good agreement with that of

Beni et al. [20] who reported that in the HAZ region of the IF steel peak temperatures are experienced for the longest period of time. This consequently leads to austenite grain growth and finally larger austenite grain leads to the formation of larger ferrite grains. The region close to base metal is the intercritical heat affected zone (ICHAZ) and adjacent to fine grain heat affected zone (FGHAZ) is shown in Fig. 5e;

**Fig. 6** SEM micrographs of **a** HAZ on the IF steel side, **b** ICHAZ, **c** FGHAZ, and **d** CGHAZ on the HSNb steel side



it consists of martensite packets at ferrite grain boundaries, as clearly revealed in the SEM image shown in Fig. 6b. This is ascribed to peak temperatures attained in ICHAZ that exists between  $A_{c1}$  and  $A_{c3}$ . The region lying in between ICHAZ and CGHAZ of the HSNb steel side is called fine grain heat affected zone (FGHAZ) on the HSNb steel side as shown in Fig. 5f. The FGHAZ on the HSNb steel side consists of finer martensite as shown in Fig. 6c. The region close to the fusion zone is called the coarse grain affected zone (CGHAZ) as exhibited in Fig. 5g. The CGHAZ of the HSNb steel side consists of coarse martensite as exhibited by Fig. 6d. The formation of martensite of different morphologies in the FGHAZ and CGHAZ regions is attaining peak temperatures above  $A_{c3}$ , resulting in the formation of the austenitized structure during the welding. During welding, FZ is melted and resolidified, resulting in the formation of cast structure with columnar grains as shown in Fig. 5h. The martensite formation could be attributed to the higher cooling rate and short welding time which induced the quenching effect [5]. The microstructure of the FZ at different welding currents is shown in Fig. 7a, c. It is observed that different morphologies of martensite are formed at both the welding currents (7 kA, 9 kA) due to variation in the heat input. The magnified view of the FZ microstructure at a lower current of 7 kA is shown in Fig. 7b that consists of lath martensite. However, it appears that at a higher current of 9 kA there is a variation in the morphology and orientation of martensite as shown by the magnified view of Fig. 7d. As the welding current increases the heat input increases, thereby there

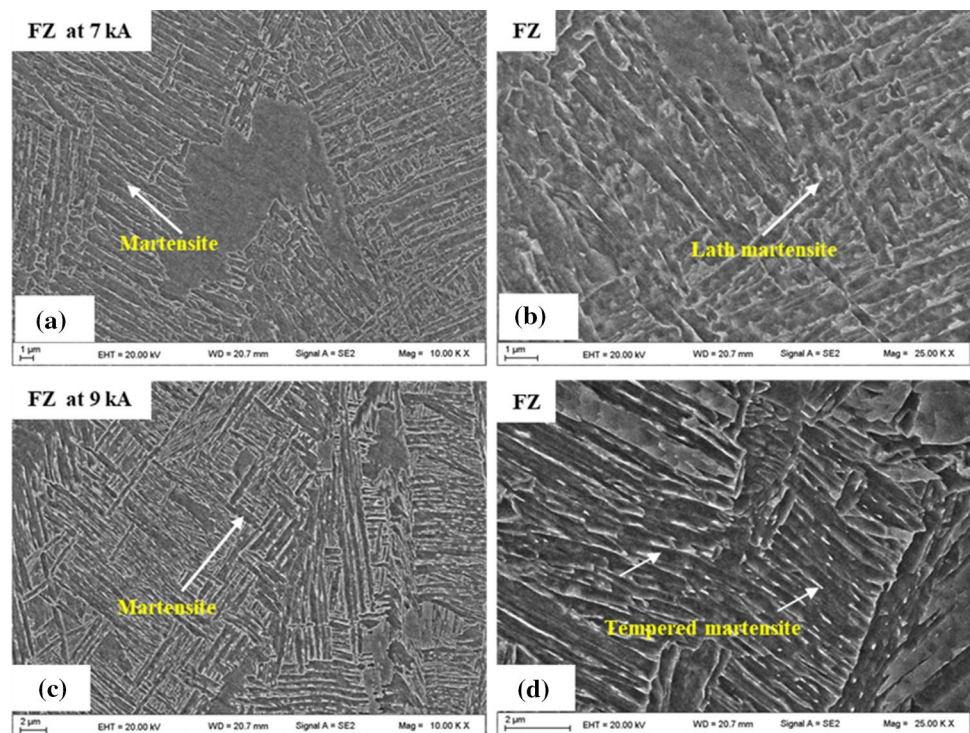
is a reduction in the rate of cooling of the molten metal. Thus, the amount of total heat stored in molten weld metal increases because of higher heat input. As the welding current increases, the cooling rate of the fusion zone lowers down, and hence there is a possibility of martensite tempering during the cooling process. Similar results have been shown by previous researchers [20–22].

### 3.2 Microhardness Profile

Figure 8a, b show the microhardness profiles of the IF/HSNb joints obtained at different welding currents (7 kA, 9 kA). The hardness gradually increases from base metal to HAZ followed by a gradual drop in the FZ due to the homogenization of chemistry of steels at both the welding currents. The hardness profile of the HSNb steel side at both welding currents (7 kA, 9 kA) exhibits higher hardness values than that of the IF steel side. However, the average hardness of the fusion zone corresponding to the 9 kA welding current as shown in Fig. 8c is lower than that of the 7 kA.

This could be attributed to the increase in the extent of martensite tempering due to higher heat input and a lesser cooling rate [18]. The average microhardness in the HAZ of the IF steel side is lower at the higher welding current (9 kA) due to the coarsening of ferrite grains unlike that of lower welding current (7 kA) as shown in Fig. 8d. These results are in good agreement with the reports of Ghosh and Pal, Khan et al. [15, 23].

**Fig. 7** SEM micrographs of **a** fusion zone at 7 kA, **b** magnified view of fusion zone shown in **(a)**, **c** fusion zone at 9 kA, and **d** magnified view of fusion zone shown in **(c)**



### 3.3 Performance of the Spot-Welds Under Tensile-Shear Loading

Figure 9 shows the typical load-extension plots of the IF/HsNb joints at different welding currents. The resulting nugget diameters, maximum tensile-shear load, and extent of energy absorbed are presented in Table 4. It is observed that load-bearing capacity and energy absorbed by the joints increased with an increase in welding current owing to the resulting higher weld nugget diameter. According to the American Welding Society (AWS), the minimum nugget diameter to ensure pull out the failure of the joints is

$$D_{cr} = 4\sqrt{t} \quad (1)$$

Here  $D_{cr}$  refers to the critical nugget diameter of the joint and  $t$  refers to material sheet thickness. The critical nugget diameter ( $D_{cr}$ ) resulting from the Eq. (1) is 4.36 mm. The obtained nugget diameters out of the current welding operations are higher than  $D_{cr}$ .

### 3.4 Performance of the Spot-Welds Under Cyclic Loading

Figure 10a shows fatigue life plots of the IF/HsNb joints at two different welding currents. It is observed that the general shape of the curve is similar at both the welding currents. As expected, the number of cycles to failure increases as the maximum load decreases. It is observed that the fatigue life

of the joints in the range of  $10^4$ – $10^6$  cycles increases with a smaller decrease in the maximum load ( $P_{max}$ ). Beyond  $10^6$  cycles up to the endurance limit, there is a substantial increase in fatigue life with a slight reduction in the maximum load at both the welding currents. It is noteworthy to mention that the joint with lower nugget diameter (4.84 mm) has achieved the endurance limit at a higher applied load of 2.07 kN as compared to that of joints with higher nugget diameter (6.63 mm), at a applied load of 1.25 kN. To have a better understanding of the effect of nugget diameter on the fatigue strength of the IF/HsNb joints, the maximum load ( $P_{max}$ ) versus number of cycles to failure ( $N_f$ ) data was expressed in terms of stress amplitude versus number of reversals to failure by estimating the shear stress using Eq. (2). A Basquin kind equation has been used to fit the obtained fatigue data which is taken from [23]. Figure 10b shows the plots of shear stress amplitude as a function of the number of cycles to failure. It is observed that, as the shear stress amplitude increases the number of cycles to failure decreases for the joints at both the nugget diameters. It is clearly observed that the joint with lower nugget diameter (4.84 mm) exhibits more fatigue strength than that of joint with higher nugget diameter (6.63 mm). The fatigue life of spot welded joints can be controlled by several factors: (i) It was earlier discussed in the microstructural analysis of the spot-welded joint that elongated ferrite grains form in both the joints (for lower and higher current), however the grain size is relatively smaller for the 7 kA specimens due to faster cooling. The smaller grain size in the HAZ of IF steel



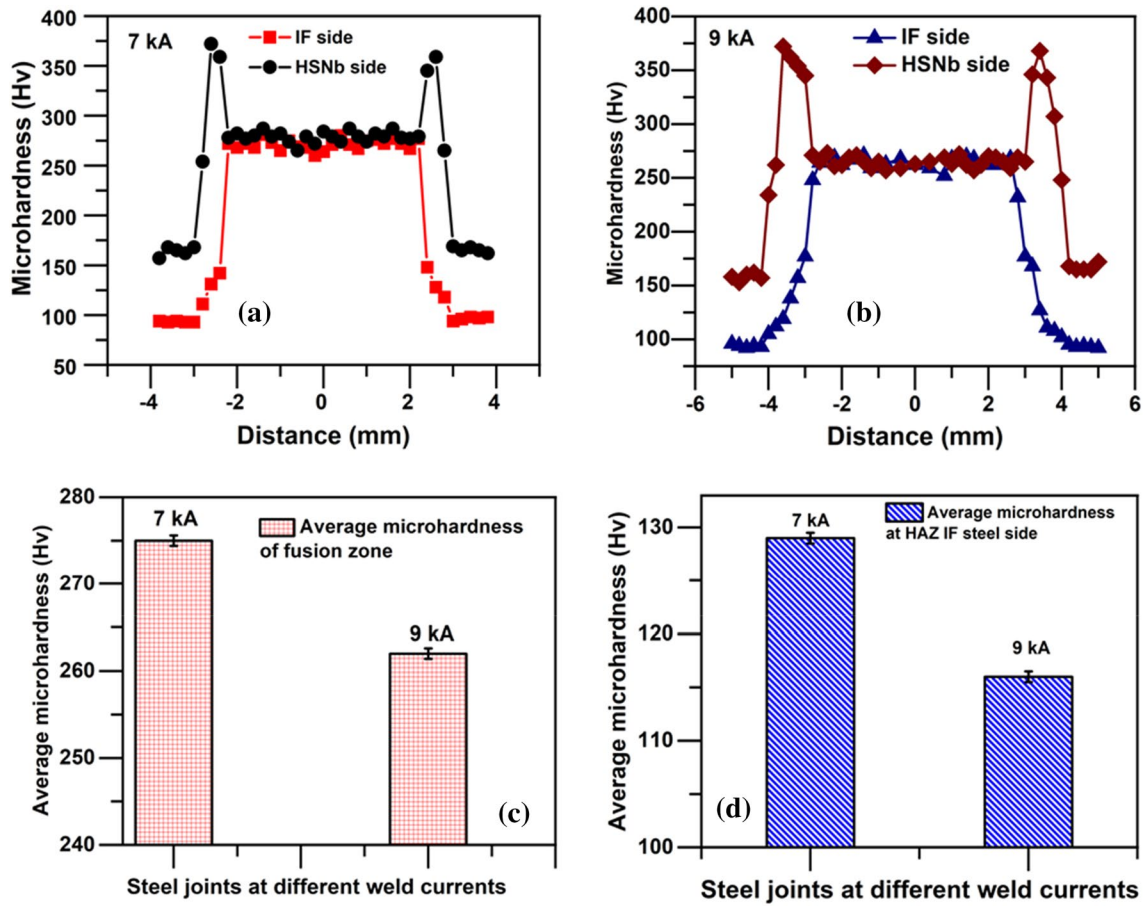
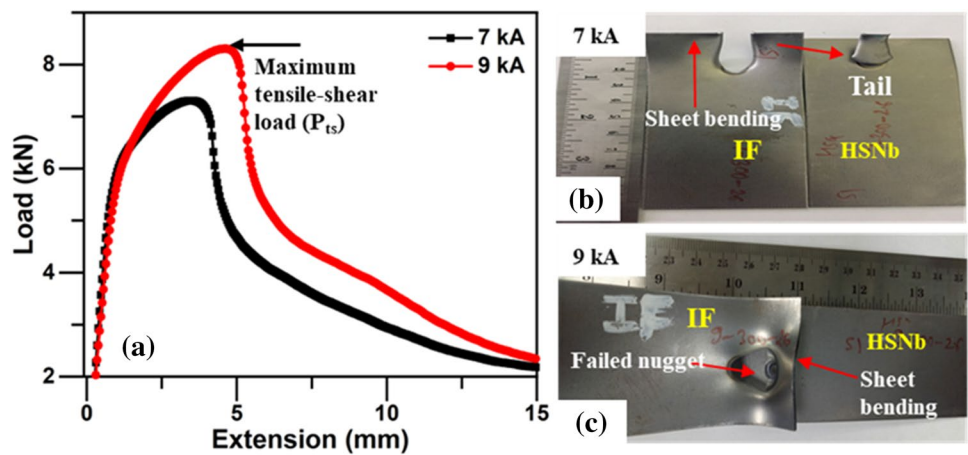


**Fig. 8** **a** Microhardness profile of the IF/HSNb steel joints at welding current of 7 kA, **b** Microhardness profile of the joints at welding current of 9 kA, **c** Average microhardness in the fusion zone, and

**d** Average microhardness in the HAZ of the IF steel side at welding currents of 7 kA and 9 kA

**Fig. 9** **a** Load-extension plots at different welding currents, **b** pull out failure of the joint at 7 kA, and **c** pull out failure of joint at 9 kA under static loading



side (7 kA) causes higher microhardness and thereby longer fatigue life as compared to that of 9 kA specimen (possessing lower microhardness). The ferrite morphology of the HAZ is regarded as quasi-polygonal in nature for both the welding currents. The polygonality however varied for the

joints obtained at 7 kA and 9 kA. The aspect ratio of the ferrite grain for the 7 kA specimens is measured as 2.93 while it is 2.59 for the 9 kA specimens. According to Krauss and Thompson, the quasi-polygonal ferrite possess higher dislocation density than the equiaxed grains due to the presence

**Table 4** Peak loads at different welding currents

Weld current (kA)	Nugget diameter (D) (mm)	Average maximum tensile-shear load ( $P_{ts}$ ) (kN)	Energy absorbed at failure (J)
7	4.84	7.2	23.45
9	6.63	8.3	30.86

of numerous sub-boundaries [24]. Hence it can be postulated that the effective dislocation density in the HAZ of the 7 kA specimen is more due to higher aspect ratio of ferrite grain. This fact further confirms the higher microhardness and thereby superior fatigue performance of the 7 kA welded specimens. (ii) Another aspect that has a significant role in fatigue performance is the residual stress [25]. Residual stresses generate in the joints due to the thermal cycling and electrode pressure during the welding process. Therefore, the measurement of residual stresses is carried out (using the X-ray diffraction method) in HAZ of IF steel side at different welding currents. The residual stress is measured particularly in this location because the joints corresponding to different welding currents fail from HAZ of the IF steel side under cyclic loading. Faster cooling rate at 7 kA causes residual compressive stresses ( $-211 \pm 3.5$  MPa) in the HAZ of IF steel (location of failure) side. In contrast, 9 kA welding current causes tensile residual stresses ( $17 \pm 2.2$  MPa). The compressive residual stress aids in reducing the effective applied stress during the cyclic loading of the joints while for 9 kA specimens the phenomenon is the opposite. Hence, the 7 kA specimens experience longer fatigue life as compared to that of 9 kA specimens. (iii) The specimen nugget geometry perhaps also bears a significant role in controlling fatigue performance of spot-welded joints of IF/HSNb steel

sheets. The inherent notch present at the interface of the two sheets is the location of higher stress concentration lying in the HAZ at the vicinity of weld nugget. The failure location for the current set of specimens has been discussed in detail in a later Sect. 3.5. The location of failure and average HAZ hardness have been illustrated in Fig. 10a, b. The results are in good agreement with that presented by Khan et al. [23]. The sheet thickness reduction due to electrode indentation is more pronounced in the case of higher welding current (9 kA) at both IF and HSNb steel side of the spot-welded joints as compared to that at lower welding current (7 kA). The sheet thickness reduction caused on both IF and HSNb side has a cumulative effect on the fatigue performance of the joints. The effective nominal stress increases at the joints due to more thickness reduction at higher welding current (9 kA) enhancing the initiation of a fatigue crack. Overall it can be considered that the performance of spot-welded joints is governed by several independent and dependent variables. The independent variables include welding current, welding time, electrode force, and sheet thickness; while the dependent variables are nugget diameter, sheet thickness reduction due to electrode indentation, variation in microstructural morphology, microhardness, residual stresses, and geometric factors of the weld nugget.

$$\tau = \frac{4P_{max}}{\pi D^2} \quad (2)$$

Here  $\tau$  refers to shear stress acting on the cross-section of the joint (MPa), ( $P_{max}$ ) refers to maximum load (N), and D refers to nugget diameter (mm).

$$\Delta\tau/2 = \tau_1(2N_f)^b \quad (3)$$

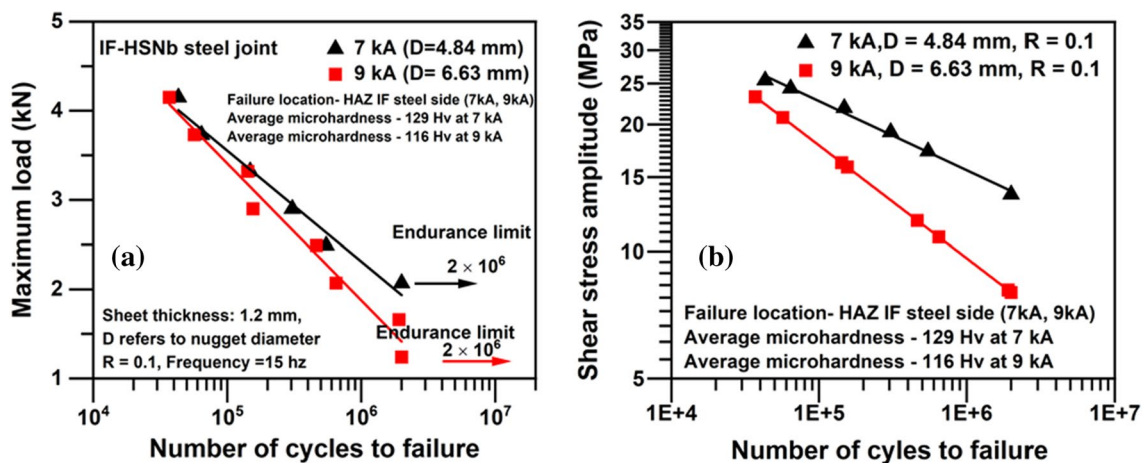


**Fig. 10** a Fatigue life plots, b shear stress amplitude versus number of cycles to failure of the IF-HSNb spot-welded joints at different nugget diameters

$\Delta\tau/2$  refers to shear stress amplitude,  $b$  is known as cyclic stress exponent,  $\tau_1$  refers to shear fatigue strength coefficient, and  $2N_f$  refers to number of stress reversals.

Two different types of failures are recognized during fatigue testing as shown in Fig. 11. At higher loads and lower number of cycles to failure, weld nugget pullout occurred. While at lower load and a higher number of cycles to failure eyebrow type fracture takes place. Finally, at the endurance limit, no visible cracks are observed on the fatigue tested samples. The fatigue failure of the joints mainly initiated from the HAZ of the IF steel side. The strength of the IF steel is less compared to that of HSNb steel and therefore in all the cases the fatigue failure is initiated from the IF steel side. The IF steel with 1.2 mm sheet thickness thus acted as the governing material for such type of dissimilar joints. Since the thickness is similar for both dissimilar materials (IF and HSNb steels); the crack initiates at the sheet having the lowest strength and hardness. However, the preferred location of crack propagation is along the lowest thickness region caused due to electrode indentation.

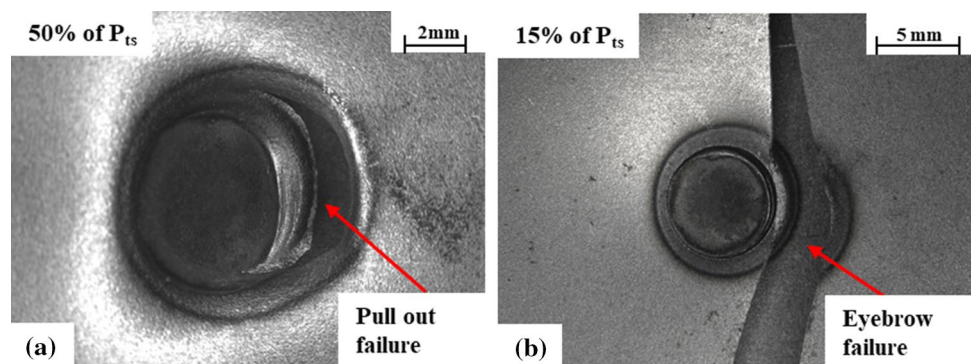
### 3.5 Post Failure Examination

The fractographic features of the specimens failed under static loading are examined. The features of the fractured surface have been observed at the inner region of the weld

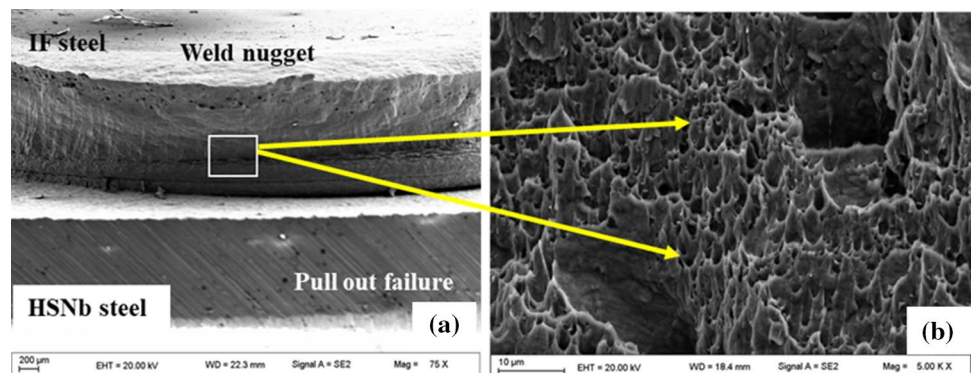
nugget as shown Fig. 12a where crack initiation takes place. It is observed that shear dimples are predominant in the fractured surface appeared as shown in Fig. 12b at a welding current of 9 kA. This represents that the fracture mechanism is ductile and tensile in nature at the material levels, while the global mode of loading is of shear type. These results are in good agreement with that of earlier works [5].

Figure 13 represents the fractographic features of the failed specimens under the cyclic load of 2.90 kN welded at higher current (9 kA). The fracture surface topography was examined near to the notch tip and at the centre of the weld nugget. In most of the cases on the failed surfaces of the IF steel side, a combination of intergranular fracture, striations, void nucleation and growth, secondary cracks are observed on the fatigue fractured surface in Fig. 13b–d. The occurrence of intergranular fracture on the IF steel fatigue is attributed to the crack growth under asymmetric slip by strongly localized plastic deformation at the grain boundaries. The factors such as temperature strain rate and range, deposition of interstitial elements at the grain boundary are also responsible for the occurrence of intergranular fracture [26]. The fatigue failure examination on the IF steel surface of the welded joints reveals that the growth of the cracks occurred by different phenomena with the variation of the applied load. The fatigue failure behaviour of the spot-welded joints is governed by stress concentration at the notch root at sheet interface, and notch size.

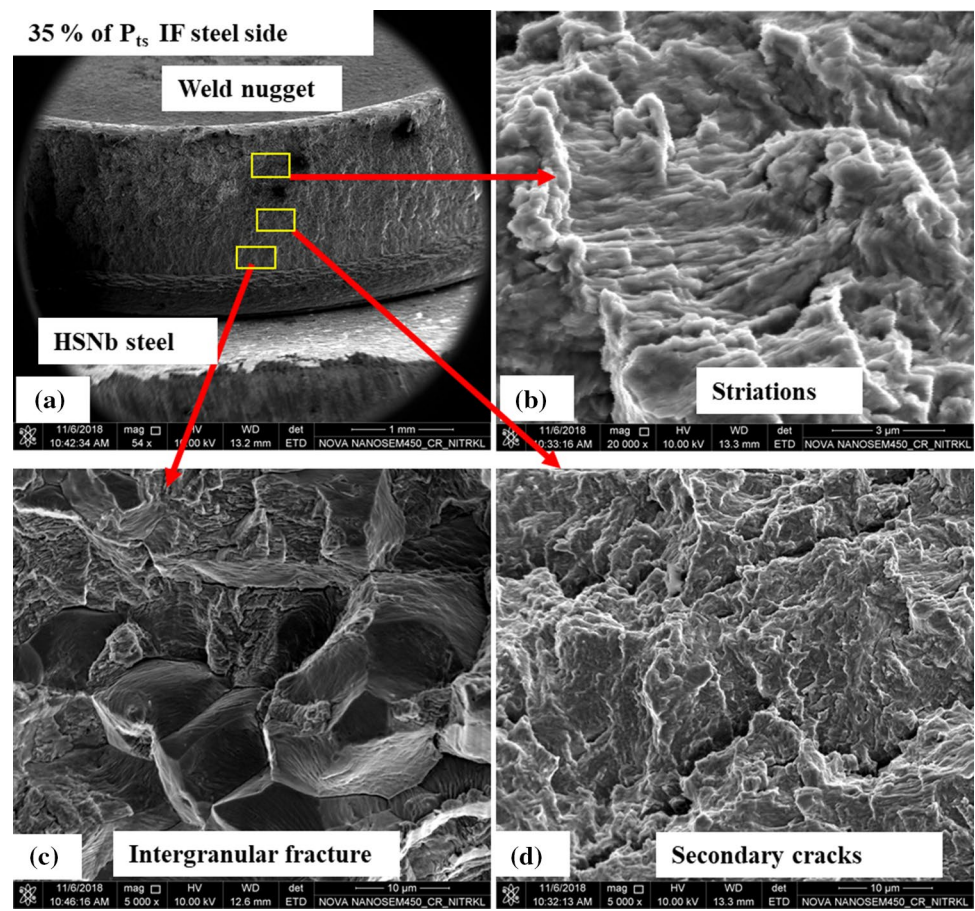
**Fig. 11** Macro views of the specimens failed under cyclic loading: **a** failed specimen at 50% of maximum tensile-shear load ( $P_{ts}$ ) **b** failed specimen at 15% of maximum tensile-shear load ( $P_{ts}$ )



**Fig. 12** Fractographic features of the joint failed under tensile-shear loading at higher welding current (9 kA): **a** low magnification image, **b** formation of shear dimples



**Fig. 13** Typical fracture surfaces of the failed specimens under cyclic load of 2.90 kN welded at higher current (9 kA): **a** low magnification image indicating different zones of fatigue failure, **b** striations, **c** intergranular fracture and **d** formation of secondary cracks



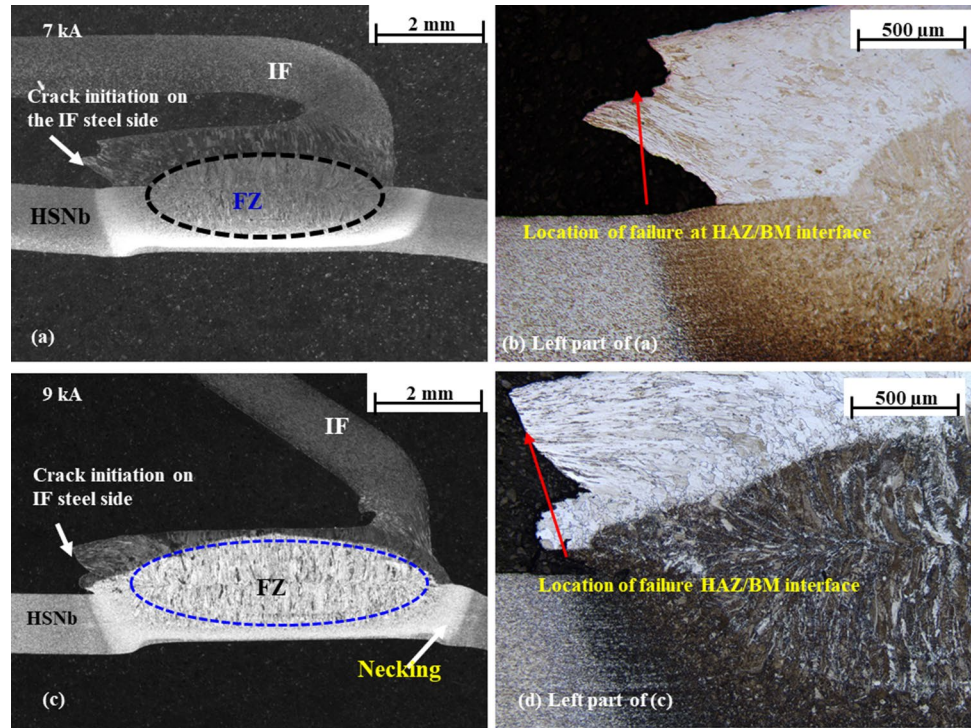
The fatigue fracture mechanism of the spot-welded joint could be classified into two categories namely (a) crack evolution cycle by cycle, (b) Cumulative crack damage with the crack growth. In this stage, the fatigue damage gathers during several numbers of cycles before the crack growth takes place. The formation of ductile striations in the fractured surface is because of the plastic blunting process, that controls the growth. However, secondary crack formation, plastic tearing could probably be attributed to the cumulative damage process. The process of crack growth is influenced by several factors such as material properties, microstructural heterogeneities (like the variation in grain size of HAZ), interactive effects of load variables, etc.

Figure 14 represents the cross-sectional views of the failed spot-welded TS specimen of IF-HSNb microalloyed steel joints under static loading at different welding currents. It is observed that the failure of the joints initiated on the IF steel side at both welding currents. Significant necking associated with grain flow occurred in the base metal due to a higher degree of plastic deformation in the joint as observed at the higher welding current (9 kA) owing to their higher weld nugget diameter. The failure initiated at the HAZ/base metal interface of the IF steel side because

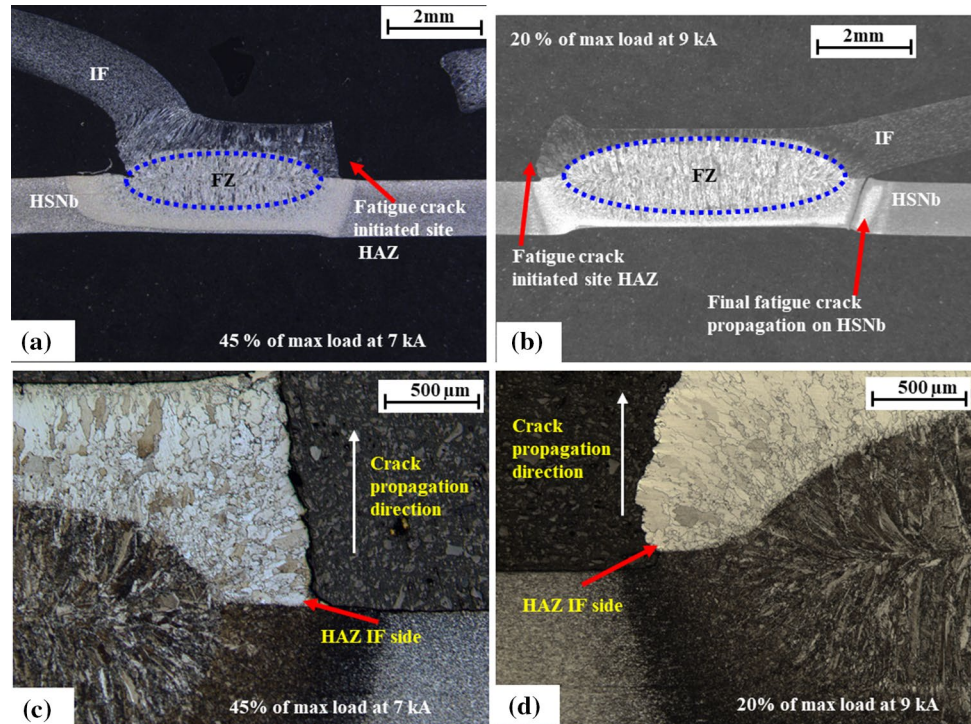
of its lower hardness and strength compared to that of other locations. Therefore, the location of the failure of joints is governed by the strength and hardness values in different zones of the weld.

Figure 15a–d represents the typical cross-sectional views to understand the location of failure of the spot-welded specimens failed under cyclic loading. At higher loads and lower number of cycles as shown in Fig. 15a at 45% of maximum tensile-shear load ( $P_{ts}$ ) at a lower welding current of 7 kA, it is observed that fatigue cracks initiated from the interface of the two sheets lying in the HAZ of the IF steel side and then crack propagates through thickness of the sheet and finally appears on the outer surface as shown in Fig. 15b. At lower loads and a higher number of cycles, as shown in Fig. 15c at higher welding current of 9 kA, it is observed that fatigue cracks initiated at the interfacial region of the two sheets in the HAZ of the IF steel side and finally, crack just propagates in the thickness direction few micrometers and then appears on the surface by complete propagation of the fatigue cracks along circumference of the weld nugget. The tearing completes into the base metal through the width direction of the sheet as shown in Fig. 15d. It is noteworthy to mention

**Fig. 14** **a** Macro-view at 7 kA, **b** micro-view at 7 kA, **c** macro-view at 9 kA, and **d** micro-view at 9 kA of the failed spot-welded specimens under static loading



**Fig. 15** **a** Macro-view at 7 kA, **b** macro-view at 9 kA, **c** micro-view at 7 kA, and **d** micro-view at 9 kA of the cross-sections of fatigue failed IF-HSNb spot-welded joints



that at a lower welding current of 7 kA at higher loads, no fatigue cracks are observed on the HSNb steel side as well as at higher welding current of 9 kA at lower loads final fatigue cracks are observed on the HSNb steel side.

### 3.6 Mechanism of Failure of the Joints Under Fatigue Loading

Figure 16a shows the macrostructure of the typical cross-section of the joint. It shows circumferential notch root

present at the interface of the two conjugated steel sheets before cyclic loading lying in the HAZ IF steel side. The notch tip acts as a preferential site for the initiation of crack under fatigue loading. Figure 16b exhibits the macrostructure of the joint, which has experienced 20% of the number of cycles of failure under fatigue loading. It is observed that initially there forms a small angular opening at the notch tip which acts as pre-crack at the end of sheet separation during the fatigue loading. The crack has initiated from the sharp notch tip surface at the interface of upper and lower conjugated sheets on the IF steel side. The crack initiation is governed by the triaxial nature of stresses applied to the joint, stress concentration, and notch size. It provides a preferential path for crack propagation at an angle of  $105^\circ$  on the IF steel side in the thickness direction. The macrostructure of the joint at 50% of the number of cycles to failure is exhibited in Fig. 16c. It is observed that the crack propagation takes place in the thickness direction on the HAZ IF steel side and finally appears on the surface by propagating through the lower sheet on the HSNb steel side in the through thickness direction. Figure 16d shows the final fracture of the joints at 40% of maximum tensile-shear load showing the final separation of upper and lower legs from the weld nugget.

The interrupted fatigue tests are carried on the specimen at higher welding current (9 kA) with higher nugget diameter (6.63 mm) at a constant load of 3.32 kN to determine the crack initiation and propagation direction. A

magnified view of the sharp notch present at the interference of the IF-HSNb conjugated sheets at 9 kA is shown in Fig. 17a. Figure 17b shows the magnified view of the primary crack initiation from the sharp notch present at the interface of the two sheets, lying in the HAZ IF steel side of the joint welded at 9 kA. As the applied load reaches saturation limit, fatigue the crack propagates through thickness direction in the IF steel side as shown in Fig. 17c. Figure 17d exhibits the propagation of the fatigue crack in the width direction. On the other hand, fatigue crack propagates in the HAZ of the HSNb steel side through complete thickness propagation and growth. Figure 17e, f exhibit the complete failure of the specimen subjected to cyclic loading at 9 kA, after attaining the maximum number of cycles at 3.32 kN. As the upper and lower legs get complete tear. The cracks completely penetrate into the base metal in the IF steel side experiencing plastic deformation. Figure 18 shows the optical micrographs along with the magnified views of the specimens subjected to fatigue testing at constant load of 3.32 kN and 20% of total number of cycles to failure. It is evident from Fig. 18a, b that no fatigue crack initiated at the joint welded at lower current (7 kA) as compared to the joints welded at higher current (9 kA) where fatigue cracks are visible as shown in Fig. 18c, d. It shows that there is delay in fatigue crack initiation at 7 kA specimens as compared to that of 9 kA specimens.

**Fig. 16** a macrostructure of the typical cross-section of the joint before fatigue testing at 9 kA welding current, b 20% of  $N_f$ , c 50% of  $N_f$ , and d fatigue failed joint at 40% of ( $P_{ts}$ ) at higher welding current (9 kA)

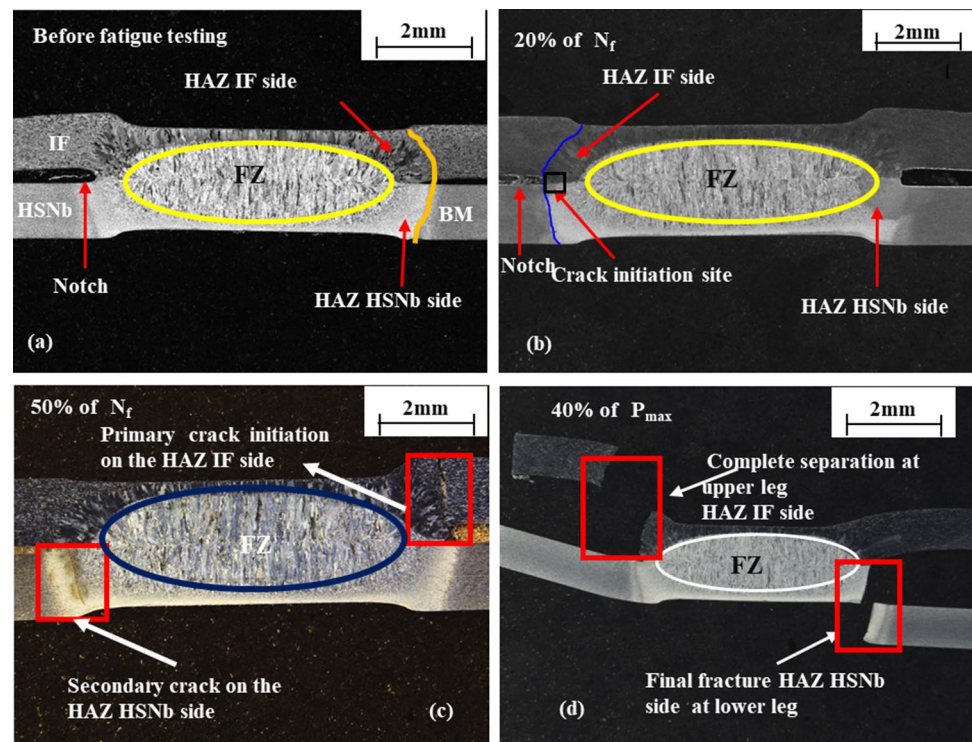
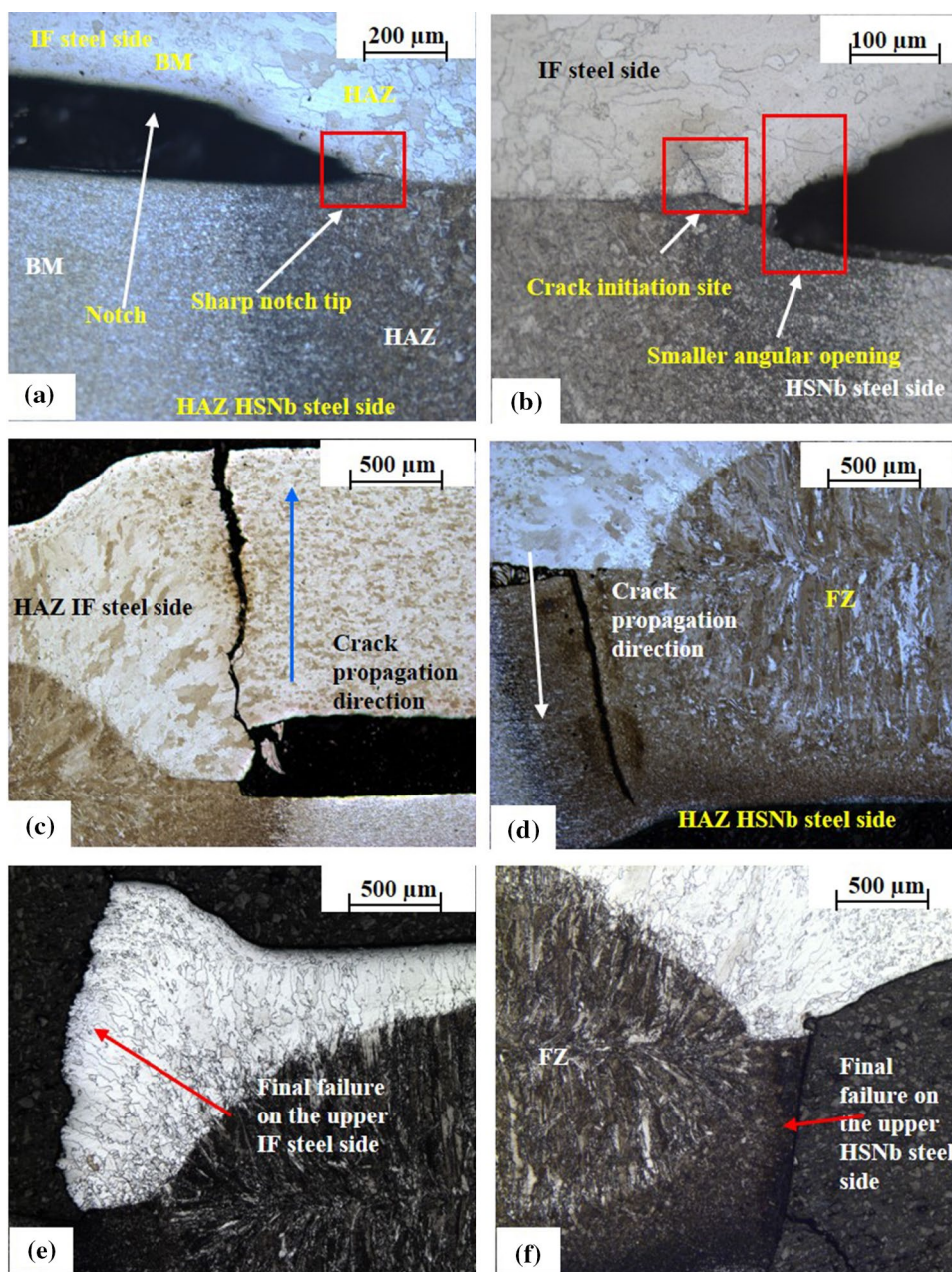


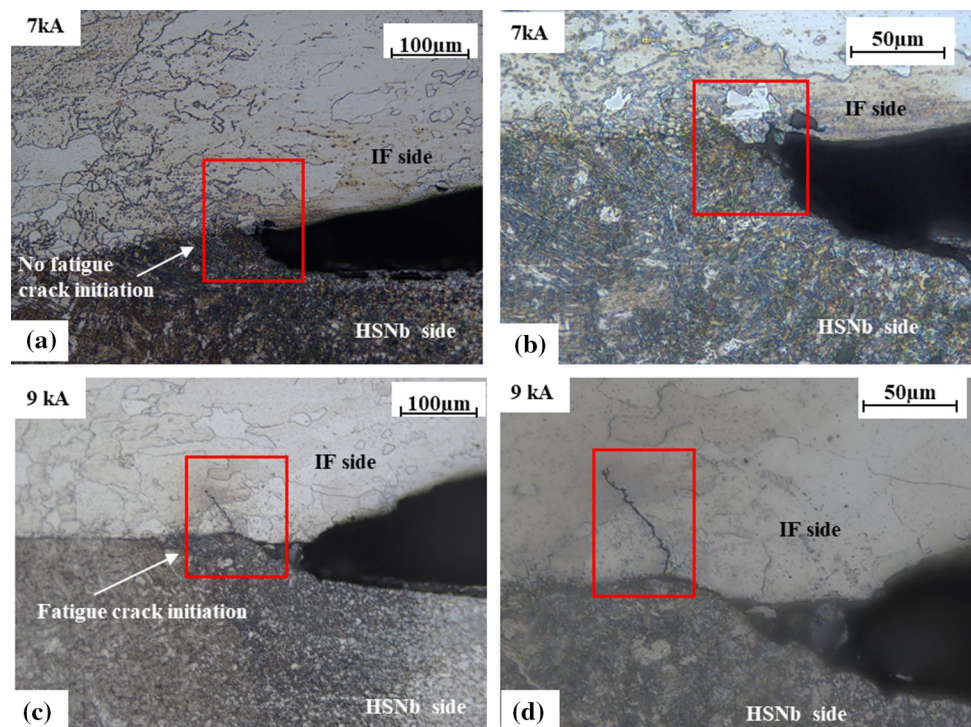
**Fig. 17** a–f magnified views of the fatigue crack initiation and its propagation of the welded joint at 9 kA welding current



## 4 Conclusions

- The microstructure of the fusion zone of the IF/HSNb joints mostly consists of lath martensite. This is attributed to the higher cooling cycle, and shorter weld time inducing quenching effect. The microhardness profiles at two different welding currents show that hardness is maximum in the HAZ of the HSNb steel side. The average hardness of FZ and HAZ (IF steel) corresponding to the 7 kA welding current is higher than that of the 9 kA welding current. The variation in the microhardness could be attributed to the microstructural variations, heating and cooling cycle of the welding process.
- The load-bearing capacity of the spot-welds under static loading corresponding to 9 kA welding current is higher than that of 7 kA. In contrast, the fatigue strength of the joints with smaller nugget diameter is higher than that of the joints with higher nugget diameter. This could be attributed to the lower microhardness in the heat affected zone of the IF steel side at higher welding current (9 kA) due to the coarsening of ferrite grains, unlike that corresponding to the lower welding current (7 kA). In association, the important factors that contribute to the superiority of fatigue performance of the IF/HSNb joints at 7 kA current include lower reduction in sheet thickness (due to

**Fig. 18** Optical micrograph of the fatigue crack initiation location (subjected to constant fatigue loading of 3.32 kN) for the joint welded at **a** 7 kA, **b** magnified view of that shown in (a), **c** 9 kA and **d** magnified view of that shown in (c)



electrode indentation), variations in microstructural morphology and presence of compressive residual stresses.

- The failure of the welded specimen under static loading initiated from the HAZ/base metal interface on the IF steel side. This is associated with significant necking and grain deformation. But, the failure of the joints under cyclic loading initiated from the heat affected zone from the IF steel side. The failure of the joints under static loading is governed by base metal strength, while under the cyclic loading it is dependent on the stress concentration at the circumferential notch present at the interference of the conjugated sheets. Hence it can be considered that governing material for the failure in the current investigation is the IF steel.

**Acknowledgements** The authors would like to acknowledge and thank Scientific Services, Advanced Material Characterization Lab and Material Welding and Joining Lab of Tata Steel Limited, Jamshedpur, India and the Management of National Institute of Technology, Rourkela.

## References

1. R. Rana, S.B. Singh, *Automotive Steels: Design, Metallurgy, Processing and Applications*, 1st edn. (Woodhead Publishing, Sawston, 2016), pp. 1–478
2. S. Acharya, K.K. Ray, Assessment of tensile properties of spot welds using shear punch test. *Mater. Sci. Eng. A* **565**, 405–413 (2013). <https://doi.org/10.1016/j.msea.2012.12.068>
3. M. Pouranvari, S.P.H. Marashi, Failure mode transition in AHSS resistance spot welds. Part I. Controlling factors. *Mater. Sci. Eng. A* **528**, 8337–8343 (2011). <https://doi.org/10.1016/j.msea.2011.08.017>
4. I. Hajiannia, M. Shamanian, M. Atapour, R. Ashiri, Evaluation of weldability and mechanical properties in resistance spot welding of ultrahigh-strength TRIP1100 steel. *SAE Int. J. Mater. Manf.* **12**, 5–18 (2018). <https://doi.org/10.4271/10-4271-05-12-01-0001>
5. M. Pouranvari, S.P.H. Marashi, Critical review of automotive steels spot welding: process, structure and properties. *Sci. Technol. Weld. Join.* **18**, 361–403 (2013). <https://doi.org/10.1179/1362171813Y.0000000120>
6. F. Rossillon, A. Galtier, J.L. Robert, M. Duchet, A. Lens, H. Oikawa, Effect of welding cycle on the fatigue behaviour of resistance spot welded dual phase steels. *Weld. World* **52**, 30–41 (2008). <https://doi.org/10.1007/BF03266680>
7. M.I. Khan, M.L. Kuntz, Y. Zhou, Effects of weld microstructure on static and impact performance of resistance spot welded joints in advanced high strength steels. *Sci. Technol. Weld. Join.* **13**, 294–304 (2008). <https://doi.org/10.1179/174329308X271733>
8. S. Daneshpour, S. Riekehr, M. Koçak, C.H.J. Gerritsen, Mechanical and fatigue behaviour of laser and resistance spot welds in advanced high strength steels. *Sci. Technol. Weld. Join.* **14**, 20–25 (2008). <https://doi.org/10.1179/136217108x336298>
9. T.K. Pal, K. Chattopadhyay, Resistance spot weldability and high cycle fatigue behaviour of martensitic (M190) steel sheet. *Fatigue Fract. Eng. Mater. Struct.* **34**, 46–52 (2011). <https://doi.org/10.1111/j.1460-2695.2010.01489.x>
10. H.M. Rao, J. Kang, L. Shi, D.R. Sigler, B.E. Carlson, Effect of specimen configuration on fatigue properties of dissimilar aluminum to steel resistance spot welds. *Int. J. Fatigue* **116**, 13–21 (2018). <https://doi.org/10.1016/j.ijfatigue.2018.06.009>
11. R.W. Rathbun, D.K. Matlock, J.G. Speer, Fatigue behavior of spot welded high-strength sheet steels. *Weld. J.* **82**, 207–218 (2003)



12. Y. Zhang, D. Taylor, Sheet thickness effect of spot welds based on crack propagation. *Eng. Fract. Mech.* **67**, 55–63 (2000). [https://doi.org/10.1016/S0013-7944\(00\)00029-1](https://doi.org/10.1016/S0013-7944(00)00029-1)
13. P. Banerjee, R. Sarkar, T.K. Pal, M. Shome, Effect of nugget size and notch geometry on the high cycle fatigue performance of resistance spot welded DP590 steel sheets. *J. Mater. Process. Technol.* **238**, 226–243 (2016). <https://doi.org/10.1016/j.jmatprotec.2016.07.023>
14. X. Long, S.K. Khanna, Fatigue properties and failure characterization of spot welded high strength steel sheet. *Int. J. Fatigue* **29**, 879–886 (2007). <https://doi.org/10.1016/j.ijfatigue.2006.08.003>
15. S. Ghosh, T.K. Pal, Combined effect of strength & sheet thickness on fatigue behaviour of resistance spot welded joint. *Fatigue Fract. Eng. Mater. Struct.* **33**, 562–574 (2010). <https://doi.org/10.1111/j.1460-2695.2010.01467.x>
16. J.H. Ordoñez, R.R. Ambriz, C. García, G. Plascencia, D. Jaramillo, Overloading effect on the fatigue strength in resistance spot welding joints of a DP980 steel. *Int. J. Fatigue* **121**, 163–171 (2019). <https://doi.org/10.1016/j.ijfatigue.2018.12.026>
17. H. Zhang, J. Senkara, *Resistance Welding Fundamentals and Applications*, 2nd edn. (CRC Press, Boca Raton, 2011), pp. 1–452
18. M. Pouranvari, A. Abedi, P. Marashi, M. Goodarzi, Effect of expulsion on peak load and energy absorption of low carbon steel resistance spot welds. *Sci. Technol. Weld. Join.* **13**, 39–43 (2008). <https://doi.org/10.1179/174329307X249342>
19. M. Pouranvari, S.P.H. Marashi, Factors affecting mechanical properties of resistance spot welds. *Mater. Sci. Technol.* **26**, 1137–1144 (2010). <https://doi.org/10.1179/174328409X459301>
20. S. Salimi Beni, M. Atapour, M.R. Salmani, R. Ashiri, Resistance spot welding metallurgy of thin sheets of zinc-coated interstitial-free steel. *Meta. Mater. Trans A.* **50**, 2218–2234 (2019). <https://doi.org/10.1007/s11661-019-05146-8>
21. B. Wang, Q.Q. Duan, G. Yao, J.C. Pang, Z.F. Zhang, L. Wang, X.W. Li, Fatigue fracture behaviour of spot welded B1500HS steel under tensile-shear load. *Fatigue Fract. Eng. Mater. Struct.* **38**, 914–922 (2015). <https://doi.org/10.1111/ffe.12289>
22. M. Pouranvari, S. Sobhani, F. Goodarzi, Resistance spot welding of MS1200 martensitic advanced high strength steel: microstructure-properties relationship. *J. Manuf. Process.* **31**, 867–874 (2018). <https://doi.org/10.1016/j.jmapro.2018.01.009>
23. M.S. Khan, S.D. Bhole, D.L. Chen, E. Biro, G. Boudreau, J. van Deventer, Welding behaviour, microstructure and mechanical properties of dissimilar resistance spot welds between galvannealed HSLA350 and DP600 steels. *Sci. Technol. Weld. Join.* **14**, 616–625 (2009). <https://doi.org/10.1179/136217109X12464549883295>
24. G. Krauss, S.W. Thompson, Ferritic microstructures in continuously cooled low- and ultralow-carbon steels. *ISIJ Int.* **35**, 937–945 (1995). <https://doi.org/10.2355/isijinternational.35.937>
25. J.K. Hong, D.H. Bae, I.S. Sohn, Assessing effects of residual stress on the fatigue strength of spot welds. *Weld. J.* **82**, 18–23 (2003)
26. M.N. James, Intergranular crack paths during fatigue in interstitial-free steels. *Eng. Fract. Mech.* **77**, 1998–2007 (2010). <https://doi.org/10.1016/j.engfracmech.2009.12.006>

**Publisher's Note** Springer Nature remains neutral with regard to jurisdictional claims in published maps and institutional affiliations.